Black hole starvation and bulge evolution in a Milky Way-like galaxy

Bonoli, Silvia ; Mayer, Lucio ; Kazantzidis, Stelios ; Madau, Piero ; Bellovary, Jillian ; Governato, Fabio

Abstract: We present a new zoom-in hydrodynamical simulation, 'ErisBH', which features the same initial conditions, resolution, and sub-grid physics as the close Milky Way-analogue 'Eris' (Guedes et al. 2011), but it also includes prescriptions for the formation, growth and feedback of supermassive black holes. This enables a detailed study of black hole evolution and the impact of active galactic nuclei (AGN) feedback in a late-type galaxy. At z = 0, the main galaxy of ErisBH hosts a central black hole of 2.6 × 106 M , which correlates to the bulge mass and the galaxy's central velocity dispersion similarly to what is observed in the Milky Way and in pseudobulges. During its evolution, the black hole grows mostly through mergers with black holes brought in by accreted satellite galaxies and very little by gas accretion (due to the modest amount of gas that reaches the central regions). AGN feedback is weak and it affects only the central 1-2 kpc. Yet, it limits the growth of the bulge, which results in a rotation curve that, in the inner ˜ 10 kpc, is flatter than that of Eris. We find that ErisBH is more prone to instabilities than Eris, due to its smaller bulge and larger disc. At z ˜ 0.3, an initially small bar grows to be of a few disc scalelengths in size. The formation of the bar causes a small burst of star formation in the inner few hundred pc, provides new gas to the central black hole and causes the bulge to have a boxy/peanut morphology by z = 0.

DOI: https://doi.org/10.1093/mnras/stw694

Originally published at:
Bonoli, Silvia; Mayer, Lucio; Kazantzidis, Stelios; Madau, Piero; Bellovary, Jillian; Governato, Fabio (2016). Black hole starvation and bulge evolution in a Milky Way-like galaxy. Monthly Notices of the Royal Astronomical Society, 459(3):2603-2617.
DOI: https://doi.org/10.1093/mnras/stw694

Monthly Notices of the ROYAL ASTRONOMICAL SOCIETY

MNRAS **459,** 2603–2617 (2016) doi:10.1093/mnras/stw694
Advance Access publication 2016 March 28

Black hole starvation and bulge evolution in a Milky Way-like galaxy

Silvia Bonoli,[1★] Lucio Mayer,[2] Stelios Kazantzidis,[3] Piero Madau,[4]
Jillian Bellovary[5,6,7] and Fabio Governato[8]

[1]*Centro de Estudios de Física del Cosmos de Aragón, Plaza San Juán 1, Planta 2, E-44001 Teruel, Spain*
[2]*Center for Theoretical Astrophysics and Cosmology, Institute for Computational Science, University of Zurich, Winterthurestrasse 190, CH-8057 Zurich, Switzerland*
[3]*Section of Astrophysics, Astronomy and Mechanics, Department of Physics, National and Kapodistrian University of Athens, 15784 Zografos, Athens, Greece*
[4]*Department of Astronomy and Astrophysics, University of California, 1156 High Street, Santa Cruz, CA 95064, USA*
[5]*Department of Astrophysics, American Museum of Natural History, Central Park West & 79th St, New York, NY 10024, USA*
[6]*Department of Natural Sciences and Mathematics, Fisk University, 1000 17th Avenue N., Nashville, TN 37208, USA*
[7]*Department of Physics and Astronomy, Vanderbilt University, PMB 401807, Nashville, TN 37206, USA*
[8] *Astronomy Department, University of Washington, Box 351580, Seattle, WA 98195-1580, USA*

Accepted 2016 March 22. Received 2016 March 5; in original form 2015 August 20

ABSTRACT

We present a new zoom-in hydrodynamical simulation, 'Eris*BH*', which features the same initial conditions, resolution, and sub-grid physics as the close Milky Way-analogue 'Eris' (Guedes et al. 2011), but it also includes prescriptions for the formation, growth and feedback of supermassive black holes. This enables a detailed study of black hole evolution and the impact of active galactic nuclei (AGN) feedback in a late-type galaxy. At $z = 0$, the main galaxy of Eris*BH* hosts a central black hole of $2.6 \times 10^6\,\mathrm{M}_\odot$, which correlates to the bulge mass and the galaxy's central velocity dispersion similarly to what is observed in the Milky Way and in pseudobulges. During its evolution, the black hole grows mostly through mergers with black holes brought in by accreted satellite galaxies and very little by gas accretion (due to the modest amount of gas that reaches the central regions). AGN feedback is weak and it affects only the central 1–2 kpc. Yet, it limits the growth of the bulge, which results in a rotation curve that, in the inner ∼10 kpc, is flatter than that of Eris. We find that Eris*BH* is more prone to instabilities than Eris, due to its smaller bulge and larger disc. At $z \sim 0.3$, an initially small bar grows to be of a few disc scalelengths in size. The formation of the bar causes a small burst of star formation in the inner few hundred pc, provides new gas to the central black hole and causes the bulge to have a boxy/peanut morphology by $z = 0$.

Key words: methods: numerical – Galaxy: bulge – Galaxy: centre – galaxies: active – galaxies: formation – galaxies: spiral.

1 INTRODUCTION

Present in nearly all spheroids (e.g. Kormendy 2004), and being the engines powering active galactic nuclei (AGN), supermassive black holes (simply black holes, from here onwards) seem to be an integral component of massive spheroidal galaxies. The tight relations between black hole mass and several properties of the host spheroid (e.g. Magorrian et al. 1998; Merritt & Ferrarese 2001; Tremaine et al. 2002; Häring & Rix 2004) give further hints that the life of black holes and their hosts are closely linked. Starting from the first analytical works on black hole 'self-regulation' (Silk & Rees 1998; King 2003), a considerable amount of effort has been spent in the last two decades in understanding the role of black hole feedback in shaping the properties of the host galaxy and controlling its own growth. Significant advance has been made by including the physics of black hole accretion and feedback (even if limited to sub-grid models) into simulations of galaxy evolution. For example, Di Matteo, Springel & Hernquist (2005) and Springel, Di Matteo & Hernquist (2005b) studied the effects of black hole (thermal) feedback during the merger of blue spiral galaxies, and found that AGN feedback has a primary role in the colour transformation of the host galaxy, by quenching star formation and causing the elliptical merger remnant to redden in a short time-scale. The combination of these results and the evidence of scaling relations between black hole mass and bulge properties, hint at the idea that is during violent, major merger events when black holes acquire most of their mass while elliptical galaxies form (e.g. Hopkins et al. 2006). On larger scales, mechanical AGN feedback in the form of jets and bubbles seems to halt cooling flows in galaxy clusters

★ E-mail: sbonoli@cefca.es

(e.g. Churazov et al. 2002; Sijacki & Springel 2006). While black hole growth and the effects of AGN feedback have been extensively explored in the case of massive early-type galaxies in clusters (e.g. Martizzi, Teyssier & Moore 2012; Dubois et al. 2013; Martizzi et al. 2014), the role black holes have played in the evolution of blue late-type galaxies evolving in smaller haloes is still largely unexplored. The small interest the community has devoted to the interplay between black holes and spiral galaxies is primarily due to the fact that late-type galaxies have small bulges and small black holes. Also, their active star formation suggests that no quenching is present in those galaxies, and thus AGN feedback is not significant.

In the effort of simulating the evolution of disc galaxies, a lot of attention has instead been given to stellar feedback. Obtaining realistic late-type galaxies has been a historical challenge for computational astrophysics since the first simulations run in the early nineties. Navarro & Benz (1991) found that the baryonic component of galaxies evolving in hierarchically growing haloes was not able to retain enough angular momentum to feature a cold disc and flat rotation curves as in realistic spirals. Those authors suggested that a proper treatment of supernova feedback (or some other form of heating) at early times would be necessary to prevent gas to lose angular momentum and catastrophically cool during galaxy interactions. Since these first simulations, our understanding of the formation of spiral galaxies has evolved significantly and, in the last few years, a large number of works from different groups has shown that proper resolution and an accurate treatment of star formation and stellar feedback are the key ingredients for creating realistic late-type galaxies (e.g. Brook et al. 2011; Guedes et al. 2011; Aumer et al. 2013; Okamoto 2013; Marinacci, Pakmor & Springel 2014; Roškar et al. 2014; Agertz & Kravtsov 2015; Murante et al. 2015). For further details on this topic, we refer the reader to the early review of Mayer, Kazantzidis & Escala (2008), the large code-comparison work of Scannapieco (2012) and the summary of all most recent developments given in section 2 of Murante et al. (2015). We discuss here only the work of Guedes et al. (2011), as that is the starting point of the new simulation presented in this paper. Guedes et al. (2011) performed a zoom-in cosmological hydro simulation of a Milky Way-size halo with a rather quiet merger history. They found that the combination of high spatial resolution (gravitational softening of 120 pc) and the use of a high-density threshold for star formation (as first used by Governato et al. 2010) and of blast-wave feedback (as in Stinson et al. 2006), contribute to the development of a clumpy and inhomogeneous interstellar medium, where overlapping SN explosions are able to inject enough energy to remove low-angular momentum material. The simulation of Guedes et al. (2011), dubbed 'Eris', is one of the first successful efforts to produce a realistic late-type spiral in a cosmological simulation.

With the new simulation that we present in this paper, 'Eris*BH*', we want to examine directly the role of AGN feedback in the evolution of late-type galaxies and explore what could be the origin and cosmological evolution of the black holes that these galaxies host. We do so by re-running the Eris simulation with the addition of black hole seeds and sub-grid physics for the growth and feedback of supermassive black holes. To isolate the effects of AGN feedback on the properties of the host galaxy, we are going to directly compare the physical properties of Eris*BH* to those of Eris.

The paper is organized as follows. Section 2 offers a brief summary of the Eris simulation and describes the technical aspects of Eris*BH*. In Section 3 we show the evolution of the black holes in the simulation, focusing in particular on the black hole of the central and most massive galaxy in the simulation. In Section 4 we show how, and to which extent, AGN feedback influences the host galaxy. Finally, in Section 5 we summarize our results.

2 THE SIMULATION

We describe here the technical aspects of the simulation. The initial conditions and the physical processes included in the simulation are the same as the ones of Eris and are briefly summarized in Section 2.1. In addition, this new simulation includes assumptions for the formation of massive black holes and follows their growth as described in Section 2.2.

2.1 Eris

Eris is a cosmological zoom-in *N*-body/smooth particle hydrodynamic (SPH) simulation that follows the evolution of a Milky Way-size halo[1] in a box of $(1\,\mathrm{Mpc})^3$, from $z = 90$ down to $z = 0$, in a *Wilkinson Microwave Anisotropy Probe* three-year cosmology (Spergel et al. 2007), with a flat universe with $\Omega_\mathrm{M} = 0.24$, $\Omega_\mathrm{b} = 0.042$, $\mathrm{h}_0 = 73\,\mathrm{km\,s^{-1}\,Mpc^{-1}}$, $n = 1$ and $\sigma_8 = 0.76$. It was run with the parallel, spatially and temporally adaptive, treeSPH-code GASOLINE (Wadsley, Stadel & Quinn 2004) for 1.5 million cpu hours. The halo was selected from the $z = 0$ output of a low-resolution and dark matter-only simulation of a $(90\,\mathrm{Mpc})^3$ volume; it was chosen to have approximately the estimated size of the Milky Way halo and to have had a rather quiet merger history, with no major mergers (above the ratio of 1: 10) after $z = 3$. The dark matter and the (initial) gas particle masses of the high-resolution region of Eris are $m_\mathrm{DM} = 9.8 \times 10^4\,\mathrm{M}_\odot$ and $m_\mathrm{gas} = 2 \times 10^4\,\mathrm{M}_\odot$. The gravitational softening length was fixed to 120 physical parsecs from $z = 9$ to the present, and evolved as $1/(1 + z)$ from $z = 9$ to the starting redshift ($z = 90$). In brief (for further technical details, see Guedes et al. 2011), the simulation includes Compton cooling, atomic cooling, metallicity-dependent radiative cooling below temperatures of 10^4K and uniform UV background. Star formation and stellar feedback are regulated by the star formation threshold n_SF (set to $n_\mathrm{SF} = 5\,\mathrm{atomcc^{-1}}$), the star formation efficiency ϵ_SF (set to $\epsilon_\mathrm{SF} = 0.1$) and the fraction of supernova energy that couples to the interstellar medium ϵ_SN (set to $\epsilon_\mathrm{SN} = 0.8$). When the conditions of the gas become favourable to star formation (according to the Schmidt law), new star particles are created following the Kroupa (2001) initial mass function, with a starting mass $m_* = 6 \times 10^3\,\mathrm{M}_\odot$ (the gas particle from which the star is created has its mass reduced by the same amount). Supernova explosions imply a deposition of metals and energy ($\epsilon_\mathrm{SN} \times 10^{51}$ erg) to the gas particles located within the blastwave radius (see equation 9 of Stinson et al. 2006), and the affected gas has its cooling shut off until the end of the supernova blastwave. Winds and stellar mass loss are also modelled as in Stinson et al. (2006).

As discussed in Guedes et al. (2011), a high value for the density threshold for star formation parameter was possible thanks to the high mass and spatial resolutions of the simulation, which allow us to resolve the clouds where star formation occurs. With this choice, star formation takes place in confined regions, giving rise to a clumpy, inhomogeneous interstellar medium, where overlapping supernova explosions inject energy in a localized manner. This

[1] The virial mass of Eris at $z = 0$ is $M_\mathrm{vir} = 7.8 \times 10^{11}\,\mathrm{M}_\odot$, and the virial radius $R_\mathrm{vir} = 234$ kpc, as given by the halo finder AMIGA (Gill, Knebe & Gibson 2004; Knollmann & Knebe 2009).

localized energy injection is able to create galactic outflows which expel low angular momentum material.

The formation of a clumpy and inhomogeneous medium seems to be the key ingredient to form a realistic late-type spiral. As described in Guedes et al. (2011), in fact, Eris is consistent with a large number of observational aspects of the Milky Way, from its structural properties to the mass content of its different components. Just to give few examples, it has a flat rotation curve, a low photometric bulge-to-disc (B/D) ratio, it falls on the Tully–Fisher and stellar-mass/halo-mass relation and it has a baryonic mass fraction within the virial radius which is 30 per cent lower than the cosmic value.

The Eris simulation did not include any sub-grid physics for the formation and evolution of supermassive black holes. In this work we want to analyse how the properties of the simulated Eris change when black hole physics is included.

2.2 Eris*BH*: Eris *plus* black hole formation, growth and feedback

Eris*BH* is a replica of Eris, but with additional prescriptions for the seeding and growth of supermassive black holes, and thermal feedback during gas accretion.

2.2.1 Seeding procedure

The origin of black hole seeds is still largely a mystery and subject of intense theoretical investigation (see, e.g. the review of Volonteri & Bellovary 2012). Thus, the criteria for inserting black hole seeds in a cosmological simulation are somewhat arbitrary. Di Matteo et al. (2008) and Booth & Schaye (2009), for example, have chosen to insert a seed black hole in every dark matter halo that rises above a given threshold in mass. This same criterion for seeding has also been used in the recent state-of-the-art cosmological simulations of Sijacki et al. (2015) and Schaye et al. (2015). Bellovary et al. (2010), instead, chose to connect the formation of black holes to star formation: gas particles with zero metallicity and with density above the set threshold for star formation, have a certain probability to be transformed into black holes rather than stars, where this probability parameter is tuned to reproduce the black hole seed halo occupation probability at $z = 3$ suggested by Volonteri, Lodato & Natarajan (2008) (which, however, is based on a very specific formation model for black hole seeds). In their cosmological simulations, Taylor & Kobayashi (2014) have adopted a similar approach, where gas particles above a certain density threshold and with zero metallicity are transformed into seed black holes.

Here, we impose both a requirement on resolution and high-density gas environment for the introduction of new black holes (but we neglect any constraint on the gas metallicity). A seed is inserted in all systems that satisfy the following conditions.

(i) Resolution requirement: the system must be bound, according to the AMIGA halo finder (Gill et al. 2004; Knollmann & Knebe 2009), and resolved with at least 10^5 particles.

(ii) Density requirement: the system must have at minimum of 10 gas particles with density above 100 atomscc^{-1}.

The resolution criterion is motivated by past works on numerical convergence of angular momentum transport in astrophysical discs simulated by SPH, which have shown that at least 10^5 particles are needed to keep a number of numerical effects under control, such as spurious hydrodynamical drags as well as enhanced gravitational torques from a noisy halo potential (Kaufmann et al. 2007). The requirement on density has been defined so that the density threshold for black hole seeding is significantly higher than the one for star formation (100 atoms cc^{-1} versus the star formation threshold of 5 atoms cc^{-1}); moreover, the choice of having a minimum of 10 gas particles with such high density ensures the presence of a high-density gas cloud.

Galaxies that satisfy these two conditions are then seeded with a black hole, provided that they do not host one already. This is effectively done by selecting the star particle that is closest to the high-density gas particle with the deepest potential and converting it into a sink particle. To estimate the mass of the seed, we calculate the number $N_{\rm gas,\,dens}$ of gas particles that have a density larger than than a fraction $f_{\rm gas,\,dens}$ of the density of the most dense gas particle in the galaxy[2]: the mass of the new black hole is then given by $N_{\rm gas,dens} \times M_*$, where$M_*$ is the mass of the converted star particle. In this way, the initial black hole mass is proportional to the number of high-density gas particles, so that the higher is the density of the gas, and the larger is the high-density region, the more massive is the newly formed black hole.

To summarize, we chose to seed only protogalaxies which are properly resolved and host clouds of high-density gas. We also chose to assign to the new black holes an initial mass which reflects the size of the high-density gas cloud.

From the beginning of the simulation down to $z \sim 3$, only six structures rise above the mass (or number of particles) limit that we have imposed. Of those, four satisfy also the condition on the gas density. At lower redshift, the gas densities become generally lower, and we stop looking for possible sites for new black holes seeds.

The first system which satisfies the seeding conditions is, at $z \sim 8.5$, the progenitor of the main galaxy of the simulation. The other three seeds are inserted in satellite galaxies at lower redshifts. Fig. 1 shows the gas density, stellar density and metallicity distributions of the systems where seed black holes are inserted. The regions of highest gas density (left-hand panels) are located around the galaxy centres and coincide with the peaks of the stellar density distribution (central panels), thus black hole seeds are naturally inserted close to the galaxy centres. In the right column we show instead the median gas metallicity as a function of distance from the newly-formed black hole seeds, and we see that the median gas metallicity decreases with increasing distance from the black hole seeds, as the metallicity is higher in the galaxy centres.

More general properties of the systems where black holes are inserted are listed in Table 1: given the imposed limit on the number of particles that a protogalaxy needs to have to host a black hole, the masses in gas, star and dark matter do not differ substantially in the four galaxies at the time each black hole is inserted. Seed masses (last column in the table) also do not differ significantly, with about one order of magnitude separating the most to the least massive seed. As a consequence, all black hole seeds are located relatively close to each other on the $M_{\rm BH}$ − stellar mass plane, slightly above the extrapolation to lower masses of the relation established observationally by more massive black holes (see left-hand panel of Fig. 7).

[2] the value of $f_{\rm gas,\,dens}$ is arbitrary, but we assumed it to be $f_{\rm gas,\,dens} = 0.5$, as that gave us seed masses close to the $M_{\rm BH}$–$M_{\rm Star}$ relation, while preserving the differences due to the diverse gas properties of the galaxies where seed black holes are inserted.

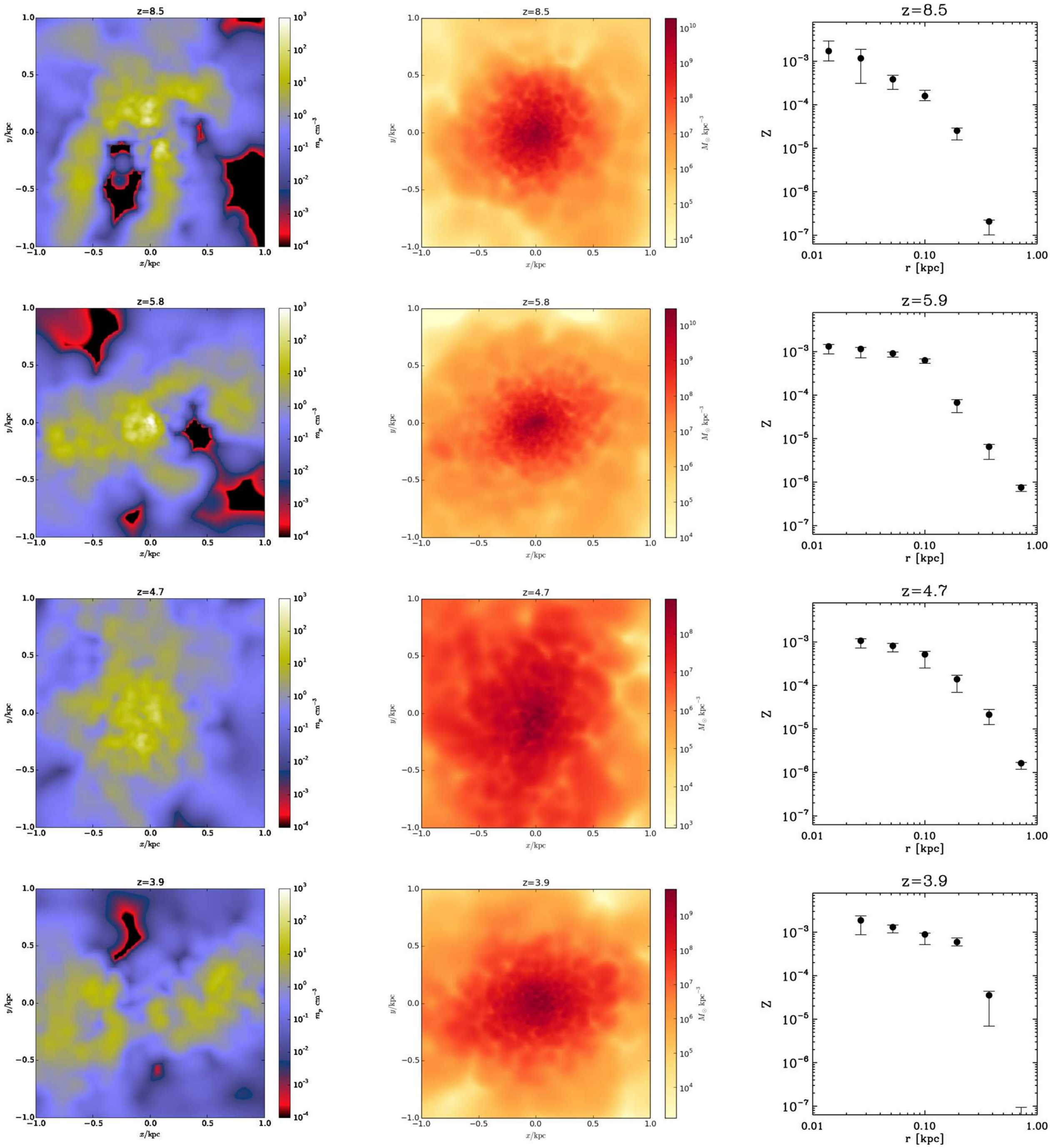

Figure 1. Galaxy properties around new black hole seeds: gas density maps (left-hand panels), stellar density maps (central panels) and median gas metallicities as a function of distance from the black hole seeds (right-hand panels, with error bars indicating the 16 and 84 percentiles of the metallicity distribution in each radial shell).

Table 1. Summary of the integrated properties of the systems that qualify as proper sites for black hole seeding, following the conditions described in Section 2.2.1. The first column gives the redshift at which the black hole is inserted in the system. The second column gives the number of gas particles that have a density higher than 100 atom cc^{-1}. The remaining columns give the virial, gas and stellar mass of the systems as well as the mass of the black hole seed.

	z - seed	$N_{\rm gas}$ > 100 atom cc^{-1}	$M_{\rm vir}$	$M_{\rm gas}$	$M_{\rm star}$	$M_{\rm BHseed}$
1	8.5	1354	7.2×10^9 M$_\odot$	7.2×10^8 M$_\odot$	1.7×10^8 M$_\odot$	8.7×10^5 M$_\odot$
2	5.8	579	4.8×10^9 M$_\odot$	5.9×10^8 M$_\odot$	1.7×10^8 M$_\odot$	1.3×10^5 M$_\odot$
3	4.7	318	7.0×10^9 M$_\odot$	1.4×10^9 M$_\odot$	2.0×10^8 M$_\odot$	7.6×10^5 M$_\odot$
4	3.9	13	6.4×10^9 M$_\odot$	7.0×10^8 M$_\odot$	1.2×10^8 M$_\odot$	0.8×10^5 M$_\odot$

2.2.2 *Black hole accretion and feedback model*

After being inserted into the simulation by converting the appropriate star particle into a sink-type particle, black holes start accreting gas isotropically from the surrounding medium, following the widely used Bondi–Hoyle–Lyttleton formalism (Hoyle & Lyttleton 1939; Bondi & Hoyle 1944; Bondi 1952):

$$\dot{M}_{\rm Bondi} = \frac{4\pi G^2 M_{\rm BH}^2 \rho}{(c_s^2 + v^2)^{3/2}}, \tag{1}$$

where ρ and c_s are, respectively, the density and sound speed of the gas, $M_{\rm BH}$ is the mass of the black hole, and v is the velocity of the black hole relative to the gas (note that, given the high spatial resolution of the simulation, we do not include here any constant factor to boost the Bondi accretion rate, as in, for example, Springel, Di Matteo & Hernquist 2005a; Booth & Schaye 2009). Growth proceeds according to equation (1), but the maximum allowed accretion rate is set to the Eddington accretion rate $\dot{M}_{\rm Edd} = (4\pi G M_{\rm BH} m_p)/(\eta \sigma_T c)$ (where m_p is the proton mass, c is the speed of light, σ_T the Thomson cross-section and η is the accretion efficiency, assumed to be 0.1), so that:

$$\dot{M}_{\rm BH} = \begin{cases} \dot{M}_{\rm Bondi} & \text{if } \dot{M}_{\rm Bondi} < \dot{M}_{\rm Edd} \\ \dot{M}_{\rm Edd} & \text{if } \dot{M}_{\rm Bondi} > \dot{M}_{\rm Edd} \end{cases} \tag{2}$$

Feedback from the accreting black hole is modelled by assuming that a fraction $\epsilon_f = 0.05$ of the radiated luminosity[3] is converted into thermal energy that heats the gas particles surrounding the black hole (32 neighbouring particles). Initially used by Di Matteo et al. (2005) and Springel et al. (2005a) in their study of the effects of black hole growth and feedback in isolated galaxy mergers, the Bondi-prescription for estimating the growth of massive black hole has been used widely in the community, also in large cosmological volumes (e.g. Di Matteo et al. 2008; Booth & Schaye 2009) (we discuss the limitation of the Bondi–Hoyle–Lyttleton formalism below in Section 3.2). Bellovary et al. (2010) have included this prescription into the GASOLINE code to study "wandering" black holes, that is, black holes that are the remnants of stripped satellite cores. As in Bellovary et al. (2010), black holes are allowed to merge if they are within one another's softening length and if they fulfill the criterion $\frac{1}{2}\Delta \boldsymbol{v}^2 < \Delta \boldsymbol{a} \Delta \boldsymbol{r}$, where $\Delta \boldsymbol{v}$ and $\Delta \boldsymbol{a}$ are the differences in velocity and acceleration of the two black holes, and $\Delta \boldsymbol{r}$ is the distance between them.

3 BLACK HOLE PROPERTIES

This section is dedicated to the analysis of the growth and evolution of the simulated black holes and the relation with the host galaxy.

3.1 Black hole growth

The upper panel of Fig. 2 shows the mass evolution of the four black holes in the simulation. Curves stop when the corresponding black hole merges with the black hole of the central galaxy (yellow symbols). The mergers (marked by the arrows) are clearly visible as 'jumps' in the yellow track. The lower panel of the figure shows again the growth of the four black holes, this time normalized by the corresponding initial mass. Growth by gas accretion is clearly limited in all black holes. The central black hole approximately doubles its mass though mergers and, since the time it was seeded into the simulation at $z \sim 8.5$, it grows, in total, only by a factor of $\sim$3, reaching a final mass of about 2.6 million Solar masses. The gas growth we find in our simulation is much more modest compared to the one obtained by Marinacci et al. (2014) in their simulations of eight Milky Way-sized haloes: all black holes hosted by their simulated central galaxies reach final masses around $10^8\,{\rm M}_\odot$. We argue that the differences in the results are likely primarily due to the different resolutions adopted in our and their simulations: Marinacci et al. (2014) have a gravitational softening of about 700 pc, while we resolve down to 120 pc. We argue that the lower resolution of their simulations implies an overestimate of the gas supply available for accretion. In our simulation, for example, the amount of gas inside $\sim$1 kpc is around $10^8\,{\rm M}_\odot$, almost an order of magnitude higher than in the inner 200–300 pc.

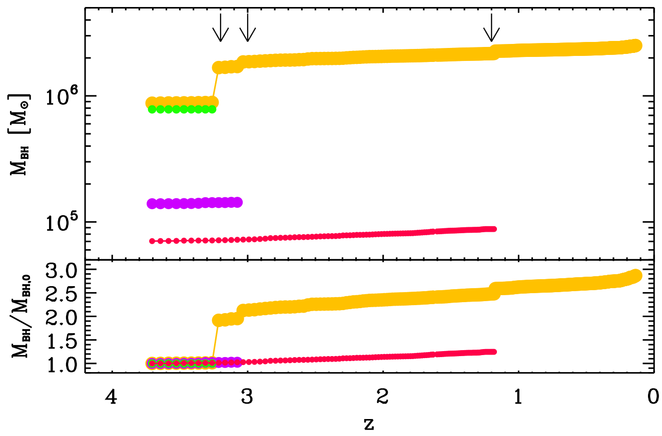

Figure 2. Upper panel: mass evolution of the four black holes in the simulation. Symbols stop when the corresponding black hole merges with the black hole of the central galaxy (yellow track). Lower panel: again mass evolution of the four black holes, but now normalized by their respective initial mass. The vertical arrows indicate the redshift at which black hole mergers take place.

Fig. 3 shows the gas accretion rate evolution of the central black hole. The red points in the upper panel indicate the median values over several timesteps (the error bars indicate the 16 and 84 percentiles of the distribution). The median accretion rates decrease only gently with redshift, and are typically quite low, $\sim 10^{-4}$–$10^{-5}\,{\rm M}_\odot\,{\rm yr}^{-1}$, but there are periodic fluctuations and peaks at higher accretion rates. While there is a global gentle decrease in the median accretion rates with decreasing redshift, at $z \sim 0.3$ the median rate increases again of about an order of magnitude: as we will discuss in the next section, this is approximately the redshift at which the disc of the galaxy is experiencing an instability event that leads to the formation of a strong bar visible in the galaxy at $z = 0$. During the process of bar formation, the gas mass and the star formation increase in the very central few hundred parsecs and the conditions around the black hole also become favourable for an increase of the accretion rate. By $z = 0$, the accretion rate has lowered again to values around $10^{-5}\,{\rm M}_\odot\,{\rm yr}^{-1}$.

In the same figure, the dashed black line indicates, for reference, which would be the instantaneous Eddington accretion rate for the black hole. We also explicitly show when the conditions of the gas around the black hole would have given a Bondi accretion rate

[3] The bolometric radiated luminosity is given by $L_{\rm Bol} = \epsilon_{\rm rad} \dot{M}_{\rm BH} c^2$, where $\epsilon_{\rm rad}$ is the radiative efficiency. For simplicity, we assume here $\epsilon_{\rm rad} = \eta$, which is a good approximation at high accretion rates when black holes are likely growing from geometrically thin and optically thick accretion discs (Shakura & Sunyaev 1973), but it might be an overestimate of the radiative power when accretion rates are highly sub-Eddington (Churazov et al. 2005; Merloni & Heinz 2008).

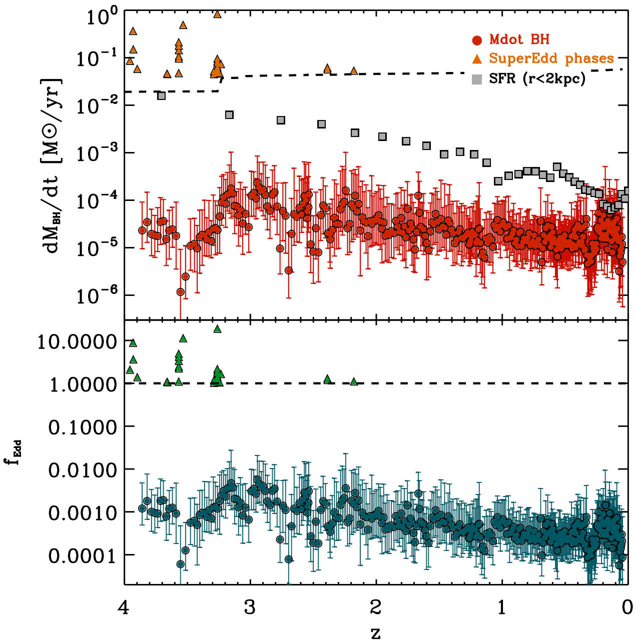

Figure 3. Upper panel: evolution of the mass accretion rate of the black hole in the main galaxy (red points), with values averaged over multiple timesteps and with error bars indicating the 16 and 84 percentiles of the distribution. The dashed black line indicates what would be the Eddington rate for the black hole at each time. The orange triangles highlight when the Bondi formula would have given a super-Eddington rate, given the gas properties around the black hole. The grey squares show the evolution of the star formation rate (multiplied by 10^{-3}) in the inner 2 kpc of the galaxy. Lower panel: evolution of the Eddington ratio, with median values taken calculated over multiple timesteps and the 16 and 84 percentiles shown with error bars. The dashed line indicates the Eddington limit and, as in the top panel, the triangles show when the accretion rates would have been super-Eddington.

higher than the Eddington limit (orange triangles): this happens rarely, and only at high redshift. However, as we do not allow super-Eddington accretion, the accretion rate in those rare cases is set to the Eddington limit. Those sporadic episodes of accretion close to the Eddington limit, at $\sim 10^{-2}\,\mathrm{M}_\odot\ \mathrm{yr}^{-1}$, might make the black hole visible already at $z \sim 6$–8 to the next generation of space telescopes, such as the *James Webb Space Telescope* (*JWST*), as the apparent bolometric luminosity associated with $\dot{M} \sim 10^{-2}\,\mathrm{M}_\odot\ \mathrm{yr}^{-1}$ at those redshifts is $m_{\mathrm{Bol}} \sim 28$–29. Assuming, in fact, that black holes in progenitors of Milky Way-type galaxies experience phases of high accretion rates even for a total of only ~10 Myr between $z \sim 8$ and $z \sim 3$, the expected duty cycle of these high-accretion events is about 1 per cent. If we further take the number density of Milky Way progenitors[4] to be $\sim 5 \times 10^{-4}\,\mathrm{Mpc}^{-3}$, the expected number of '*JWST*-visible' black holes in the redshift range $6 < z < 8$ can be as high as ~10–100 deg^{-2}.

The bottom panel of Fig. 3 explicitly shows the evolution of the Eddington ratio ($f_{\mathrm{Edd}} = \dot{M}_{\mathrm{BH}}/\dot{M}_{\mathrm{Edd}}$), which is typically between 10^{-4} and 10^{-2}. As in the top panel, the triangles show the few rare times where the Bondi formula would give accretion rates higher than the Eddington limit. By $z = 0$ the Eddington ratio reaches the lowest median values of $\sim 10^{-4}$.

Accretion rates between 10^{-5} and $10^{-3}\,\mathrm{M}_\odot\ \mathrm{yr}^{-1}$ are, conservatively, the accretion rates expected from Bondi accretion of hot gas and stellar mass loss in the centre of nearby galaxies, as discussed by Ho (2009). At $z = 0$ our simulated black hole is accreting close to those values, at $\sim 10^{-5}\,\mathrm{M}_\odot\ \mathrm{yr}^{-1}$, which corresponds to a bolometric luminosity of $\sim 10^7\,\mathrm{L}_\odot$ (assuming a radiative efficiency $\epsilon_{\mathrm{rad}} = 0.1$). This is close to the median value of nuclear luminosity of local Seyfert galaxies found by Ho (2009). As discussed in Section 2.2.2 however, the radiative efficiency is likely lower than the 10 per cent value we have adopted here, and can be as low as $\epsilon_{\mathrm{rad}} \sim 10^{-3}$–$10^{-4}$ for the accretion rates we have in our simulation at late time. At those low rates, in fact, energy from the accreting black hole is likely released as kinetic, rather than radiative, power (Churazov et al. 2005; Merloni & Heinz 2008). With significantly lower efficiencies of energy release, the luminosity of the nucleus of Eris*BH* could be several orders of magnitude lower, thus being closer to the luminosities that Ho (2009) find for a large fraction of local galaxies (including the Milky Way[5]). Had we assumed a lower value for the radiative efficiency for the phases at the lowest Eddinton ratios, the effects of radiative AGN feedback on the galaxy would have been even more modest than what we have obtained in our simulation.

In the top panel of Fig. 3 we also show the evolution of the star formation rate (SFR, multiplied by 10^{-3} for plotting purposes, and with values averaged over 10 snapshots, which correspond to about 300 Myr) in the inner 2 kpc of the galaxy. As the bulge stars dominate approximately the inner 2 kpc of the galaxy at $z = 0$ (see Section 4.2), and as most of the bulge stars are formed *in situ* (see Guedes et al. 2013), the SFR within 2 kpc from the centre is a good proxy for the SFR of the stars within the bulge. The black hole accretion rate is between 6 and 4 orders of magnitude smaller than the SFR in the bulge. As expected for a late-type galaxy, the growth rate of the central black hole is thus significantly smaller than the growth rate of the bulge. In Section 3.4 we explicitly show how this translates into black hole-galaxy scaling relations.

Given the little gas supply and the modest growth by accretion, the initial seed mass is rather important. Generalizing our results, we expect the progenitors of Milky Way-size galaxies to be hosting an intermediate-mass black hole already at $z \sim 8$. For seeds from PopIII remnants (e.g. Bond, Arnett & Carr 1984; Haiman & Hui 2001; Madau & Rees 2001; Tanaka & Haiman 2009), given the little time available before $z \sim 8$, uninterrupted growth close to the Eddington rate would be required to reach intermediate masses (unless super-Eddington accretion is possible, see, for example, Wyithe & Loeb 2012; Madau, Haardt & Dotti 2014; Volonteri, Silk & Dubus 2015). An alternative are seeds from direct-collapse, which could be already between 10^4 and $10^6\,\mathrm{M}_\odot$ at the time of formation. While the predicted number density of direct collapse black holes is quite small in some direct-collapse models (Dijkstra, Ferrara & Mesinger 2014), it is not unfeasible that a small subset of galaxies could form supermassive black holes through this channel. Given the properties of Milky Way progenitors, direct collapse black holes born in metal-free protogalaxies (e.g. Lodato & Natarajan 2006; Wise, Turk & Abel 2008; Regan & Haehnelt 2009; Johnson et al. 2011; Agarwal et al. 2012; Dijkstra, Ferrara & Mesinger 2014) are a

[4] We estimated the number density of Milky Way-type galaxies by looking in the Millennium data base [http://gavo.mpa-garching.mpg.de/Millennium/ (Lemson & Virgo Consortium 2006), using the galaxy catalogue from Guo et al. 2011] for all the galaxies that, at $z = 0$, have a stellar mass in the range $3 - 6 \times 10^{10}\,\mathrm{M}_\odot$, a B/D ratio in the range 0.1–0.5 and a dark matter halo mass in the range 6×10^{11}–$2 \times 10^{12}\,\mathrm{M}_\odot$.

[5] The estimated luminosity of the Galactic centre is $L_{\mathrm{bol}} < 10^{37}\,\mathrm{erg\,s^{-1}}$ (see, e.g. Skinner et al. 1987; Pavlinsky, Grebenev & Sunyaev 1994; Baganoff et al. 2003, and other references in Narayan et al. 1998.)

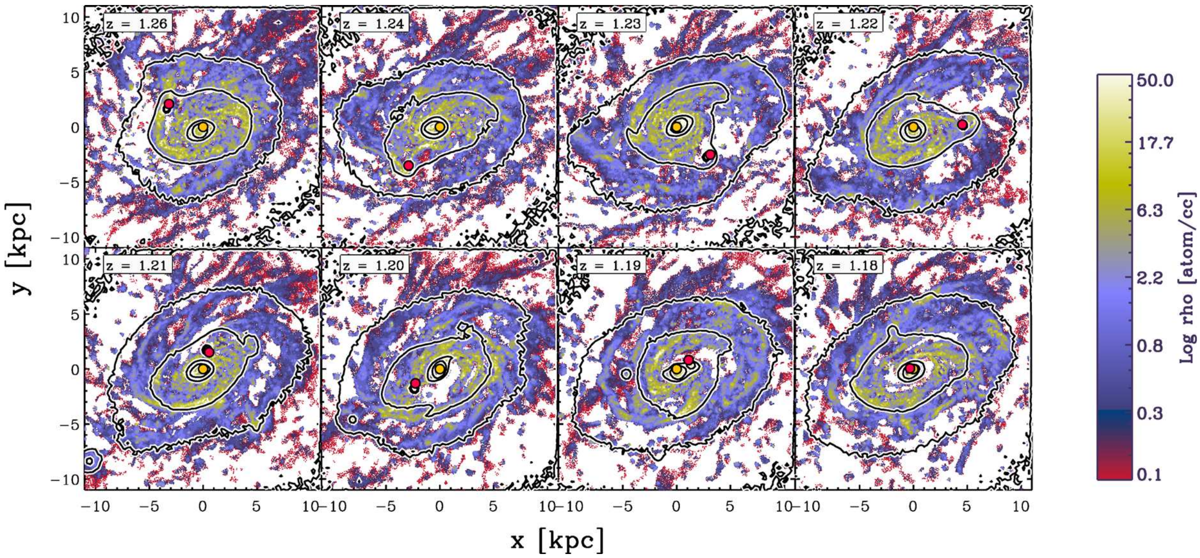

Figure 4. Time sequence of the last black hole merger in the simulation. Black holes are represented by the yellow and red bullets. The gas map is colour-coded according to the particle density. In black are overplotted stellar isodensity contours.

more plausible scenario than the direct collapse black holes formed after galaxy major mergers, as these events are only possible during mergers of much more massive galaxies (Mayer et al. 2010; Bonoli, Mayer & Callegari 2014; Mayer et al. 2015).

3.2 A discussion on the Bondi–Hoyle–Lyttleton prescription

As introduced in the methodology section, in this paper we have used a specific model for black hole accretion, the Bondi–Hoyle–Littleton model, which is simple and widely used in the literature of cosmological simulations. At the same time, though, it is known to be often inaccurate for flows in the nuclei of galactic discs, which are neither spherical and hydrodynamical, but are rather governed by the effects of gravitational torques in the redistribution of angular momentum and kinetic energy (e.g. Debattista et al. 2006; Hopkins & Quataert 2010, 2011). In particular, Hopkins & Quataert (2011) have proposed a different sub-grid model for accretion on to massive black holes in simulations that is based on the analysis of angular momentum transport in galactic discs of stars and gas, where the self-gravitating perturbation destabilizing the axisymmetric gas flow is assumed to be coming from the stellar potential only. The latter is a good approximation in our case since star formation is vigorous in the nucleus at high redshift (see Fig. 12), leading to stellar-to-gaseous mass ratio larger than 10 at distances below 300 pc from the centre already at redshift $z \sim 4$ (see Fig. 8). Hopkins & Quataert (2011) have shown that their proposed new sub-grid model captures very closely the mass inflow rates at small scales occurring in very high resolution simulations, which resolve down to $\sim$pc scales, hence close to the boundary of the accretion disc, while the Bondi model can overestimate by even more than an order of magnitude the inflow rate occurring in simulations at such scales. Since we only resolve gravity to about 100 pc scales, the size of our gravitational softening length, we can do a back-of-the-envelope calculation to estimate the accretion rate that the model of Hopkins & Quataert (2011) would give at those scales. According to their model, the mass inflow rate $\dot{M}$ on to the black hole is $\sim a M_{\rm gas}/T_{\rm orb}$, where $M_{\rm gas}$ is the gas mass at the smallest scale, $T_{\rm orb}$ is the orbital time at the same distance and a is a constant related to the amplitude of gravitational torques, which is maximum in major mergers ($a = 1$) and can be as small as $a = 0.01$ in weakly self-gravitating disc. We can apply the model to the high-redshift phase of black hole growth (z = 2–4) which is the one yielding, on average, the highest accretion rates (see Fig. 3). Assuming a = 0.01–0.1, since most of the time our galaxy does not undergo significant mergers, and taking $M_{\rm gas}$ a few times $10^7\,{\rm M}_{\odot}$ (corresponding to the values in the original Eris simulation shown in Fig. 8) and $T_{\rm orb} \sim 10^7$ yr, a typical value for the inner few hundred parsecs, we obtain $\dot{M} \sim 10^{-2}$–$10^{-1} M_{\odot}$ yr. Those values for the accretion rate are higher than the accretion rates measured in the Eris*BH* simulation, despite its adoption of the Bondi model. This is reassuring, since feedback is expected to decrease the accretion rates further, yet there is no evidence that the Bondi model employed is boosting severely the accretion rates. This suggests that in our case the accretion rates are not strongly dependent on the accretion model adopted, but they are rather bound to be low because they arise from the weak gas inflows occurring at the *resolved* scales, from few kpc to a few softening lengths. This is line with the notion that we are modelling a fairly quiescent halo that does not undergo many prominent mergers, and this seems to naturally lead to the formation of a late-type spiral with a pseudobulge. It also confirms that our general key conclusion that massive black holes in late-type spirals grow little by accretion should be quite general.

3.3 A close look to black hole mergers

As previously discussed, mergers with black holes from satellite galaxies contribute significantly to the mass-growth budget of the black hole hosted by the central and most massive galaxy of the simulation. The resolution of the simulation allows us to follow the evolution of black hole binaries down to few hundreds of parsecs. The maps in Fig. 4 show the evolution of the last black hole merger in the simulation, occurring at $z \sim 1$, with gas particles coloured according to their density and black lines indicating stellar isodensity contours. At the beginning of the sequence, the stellar core, remnant of the satellite galaxy and visible as a peak in the isodensity contours, is at a distance of a few kiloparsec from the centre of the central galaxy. As time progresses, the stellar core, hosting the secondary black hole, spirals towards the centre of the galaxy via

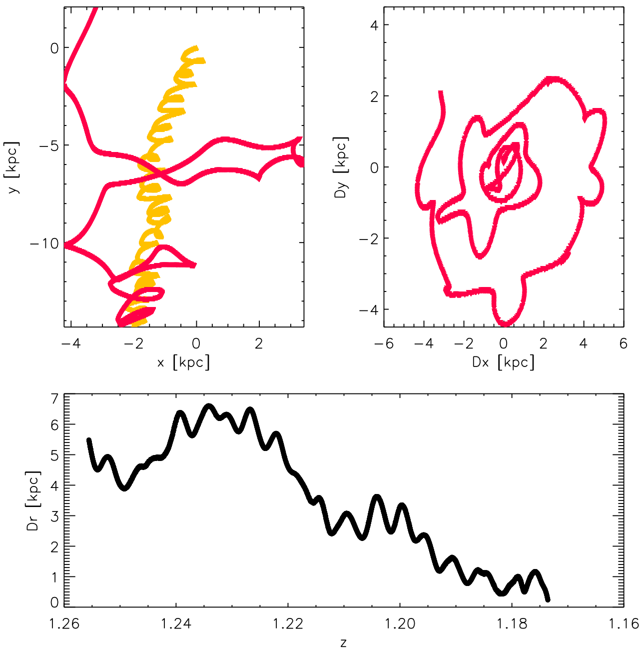

Figure 5. Details of the spatial evolution of the two black holes shown in the maps of Fig. 4. Upper left panel: evolution of the $x - y$ position of the two black holes (centred at the initial position of the primary black hole). Top right panel: $x - y$ projection of the orbit of the secondary black hole around the primary. Lower panel: redshift evolution of the separation between the two black holes.

dynamical friction. At the end of the sequence, the stellar nuclei of the two galaxies finally merge, just before the two black holes also merge, as they satisfy the criteria for merging described in Section 2.2.2. This sequence spans ∼250 Myr in the cosmology assumed here.

Fig. 5 shows quantitatively the position, separation and orbit evolution of the two black holes from several kpc scales down to the softening scale of the simulation. The upper left panel shows the $x - y$ position of the two black holes in the same time interval shown in Fig. 4, where the positions have been centred at the location of the primary black hole at the time we start tracking the binary system. While the central black hole (yellow curve) oscillates around its original position, the satellite black hole shows a typical spiralling pattern until it finally joins the central one. The top-right panel shows instead the $x - y$ projection of the orbit of the satellite black hole around the primary one and, finally, the bottom panel of the same figure shows the redshift evolution of the separation between the two black holes. In about 250 Myr the black holes go from a distance of several kpc to a separation smaller than the spatial resolution of the simulation, at which point they are assumed to merge. Such short time-scale for the evolution of the black hole binary system is consistent with the results of high-resolution merger simulations of, e.g. Mayer et al. (2007) and Chapon, Mayer & Teyssier (2013).

However, we also note that detailed numerical simulations of massive black hole mergers in circumnuclear discs have shown that the formation of a tight binary below our resolution scale of 120 pc can be delayed to up to 10^8 yr in the favourable case of major mergers (Roškar et al. 2015), and to even longer time-scales (up to a Gyr) in the case of minor mergers, due to a variety of processes such as ram pressure stripping of the secondary galaxy core surrounding the secondary black hole (Callegari et al. 2009, 2011). In any case, all black hole mergers in our simulation occur at very early times, when dynamical time-scales are still very short, possibly reassuring us that neglecting to capture the small scale dynamics is not an issue. We finally note that, with our resolution, we encounter no problems in following the black hole orbital decay directly down to the scale of the softening length, namely without having to impose an artificial drag force (e.g. Tremmel et al. 2015).

3.4 Black hole-galaxy scaling relations

Since their discovery more than 20 yr ago (e.g. Magorrian et al. 1998; Merritt & Ferrarese 2001; Tremaine et al. 2002), the tight relations between black hole mass and various properties of the host galaxies have been interpreted as an evidence of some type of co-evolution between massive black holes and their hosts. Those relations have been first defined for massive bulges or elliptical galaxies, and has not been clear whether they hold when going to low mass galaxies or galaxies with different morphologies. Recent studies have found that black holes in pseudobulges do not correlate in the same way, if at all, with galaxy properties as black holes in classical bulges (e.g. Greene, Ho & Barth 2008; Hu 2008; Jiang, Greene & Ho 2011; Kormendy, Bender & Cornell 2011; Mathur et al. 2012; Graham & Scott 2015). Studying active low-mass galaxies, Greene et al. (2008) found, for example, that black holes in pseudobulges sit on the extrapolation to lower masses of the $M_{\rm BH}$–σ relation, while they lie almost an order of magnitude below the $M_{\rm BH}$–$M_{\rm Bulge}$ relation. The different behaviour for classical bulges and pseudobulges seems to be due to the different relation between stellar mass and velocity dispersion that they follow (Gadotti & Kauffmann 2009). Kormendy et al. (2011) studied systems with dynamically-estimated black hole masses, and found evidence that no correlation actually exists between black hole masses and pseudobulges. Those authors argue that the lack of correlation is possibly due to the different history of black holes evolving in pseudobulges compared to the ones in classical bulges: black hole growth in pseudobulges is likely driven by small-scales and stochastic events and is typically highly sub-Eddington, in contrast with the growth of the most massive black holes, which is driven by large-scale dramatic events, such as the violent mergers, that are able to both efficiently feed black holes and to generate classical bulges and elliptical galaxies. The bulge of Eris*BH* has the properties of a pseudobulge rather than a classical bulge (see Section 4.2) and we can thus directly see whether our simulated black hole has properties consistent with the ones of black holes in observed pseudobulges.

In Fig. 6 is shown where the Eris*BH* central black hole sits in the $M_{\rm BH}$–σ relation (yellow bullet), compared with the observational data points compiled by McConnell & Ma (2013). We estimated the velocity dispersion for Eris*BH* using the $1/\sqrt{3}$ of the $3 - D$ velocity dispersion within 2 kpc from the centre. With this assumption, we obtain a value for σ of 109 km s^{-1}. Our calculation for the velocity dispersion gives values that are quite comparable to observational long-slit measurements of face-on nearby galaxies (Bellovary et al. 2014). The obtained value of 109 km s^{-1} is also within the errors of the velocity dispersion of the Milky Way (103 ± 20 km s^{-1}) given in the compilation of McConnell & Ma (2013). We see that Eris*BH* sits slightly below the relation, as its black hole mass is about 2/3 the mass of the Milky Way's central black hole, assuming that SgrA* is 4.1×10^6 M$_\odot$ (from the works of Ghez et al. 2008; Gillessen et al. 2009).

Fig. 7 shows instead the scaling relations between black hole mass and stellar mass (left) and between black hole mass and the bulge component of galaxies (right). Here we use as reference observational points the compilation of Erwin & Gadotti (2012) (red

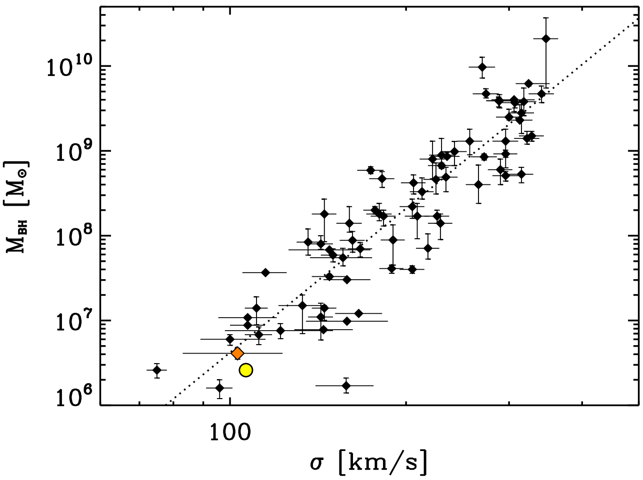

Figure 6. $M_{\rm BH} - \sigma$ plane: the black symbols are observational points from the compilation of McConnell & Ma (2013) (best fit shown by the dotted black line), the orange diamond is the location of the Milky Way while the yellow circle indicates the location of Eris*BH*.

and blue symbols, representing the location of early- and late-type galaxies, respectively). As in the previous figure, the orange diamond represent the location of the Milky Way and the yellow bullet the location of Eris*BH*. As estimates for the bulge and stellar components of Eris*BH* we use the results of a double-Sérsic fitting to the surface density profile of our simulated galaxy, as described in Section 4.2 (the values are given in Table 2). Eris*BH* sits well below both relations, even though the black hole seeds start off close to the extrapolation at lower masses of the MBH-stellar mass relation (coloured bullets in the left-hand panel): this is because the black hole accretion rates are much lower than what would be required to keep up with the star formation rate in the central region (see Fig. 3).

Having only one simulation, we can not give quantitative predictions on whether black holes in pseudobulges follow a different relation with the properties of the host (or if they do not follow any relation at all). But we note that our results on the $M_{\rm BH}$–σ and $M_{\rm BH}$–$M_{\rm Bulge}$ relations are both consistent with what is found by Greene et al. (2008), and could also fit within the picture drawn by Kormendy et al. (2011), given the slow Seyfert-like growth of our simulated black hole.

4 BLACK HOLE FEEDBACK AND ITS EFFECTS ON THE HOST GALAXY

As described in Section 2.2.2, the simulation includes also a prescription for black hole feedback: a fraction of the energy extracted in the accretion process couples thermally with the surrounding medium. This standard prescription has been used extensively in other works, and its effects led to the idea of a 'self-regulation' of black hole growth to explain the origin of the $M_{\rm BH}$–σ relation and the ejection of gas from the host galaxy and the resulting quenching of star formation (e.g. Di Matteo et al. 2005). Given that the accretion rates are generally quite small for the central black hole of our simulated galaxy, we expect the effects of feedback to be modest. We find, in fact, that the amount of energy released by the black hole is significantly lower than the one released by supernova explosions (integrating from $z \sim 3$ to $z = 0$, the total energy

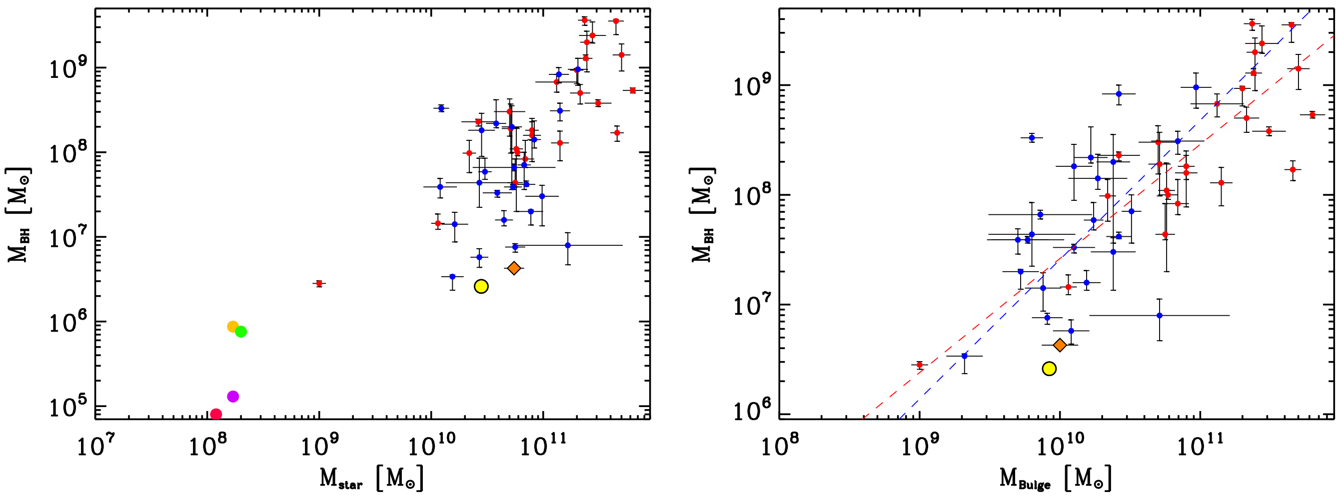

Figure 7. $M_{\rm BH}$–$M_{\rm Star}$ and $M_{\rm BH}$–$M_{\rm Bulge}$ relations. The red and blue symbols are from a compilation of Erwin & Gadotti (2012) for early-type and late-type galaxies, respectively (with fits for the $M_{\rm BH}$–$M_{\rm Bulge}$ relation shown by the dashed lines). The orange diamond is the location of the Milky Way in the plane as reported by Erwin & Gadotti (2012). The yellow circle indicates the location of Eris*BH*. The coloured bulletts in the $M_{\rm BH}-M_{\rm Star}$ figure show the location of the seeds, colour-coded as in Fig. 1

Table 2. Summary of global properties of Eris*BH* and Eris at $z = 0$. The stellar and gas masses in columns 1 and 2 refer to the total stellar and gas masses within the halo, also used to calculate the baryon fractions given in column 3. The disc and bulge masses have been obtained fitting a double Sérsic profile to the face-on surface density profile, with scale lengths given in columns 8 and 9. The last column gives the Sérsic index for the bulge, while the Sérsic index for the disc has been fixed to unity. Masses are given in solar masses, distances in kpc and velocities in km $\rm s^{-1}$.

	$M_{\rm star}$	$M_{\rm gas}$	f_b	$V_{\rm max}$	$M_{\rm Disc}$	$M_{\rm Bulge}$	B/T	$R_{\rm disc}$	$R_{\rm bulge}$	$n_{\rm s}$ (Bulge)
Eris*BH*	3.2×10^{10}	5.9×10^{10}	0.118	193.2	$2. \times 10^{10}$	8.4×10^{9}	0.29	2.9	0.4	0.9
Eris	3.9×10^{10}	5.6×10^{10}	0.121	239.2	1.9×10^{10}	1.5×10^{10}	0.44	2.3	0.3	1.2

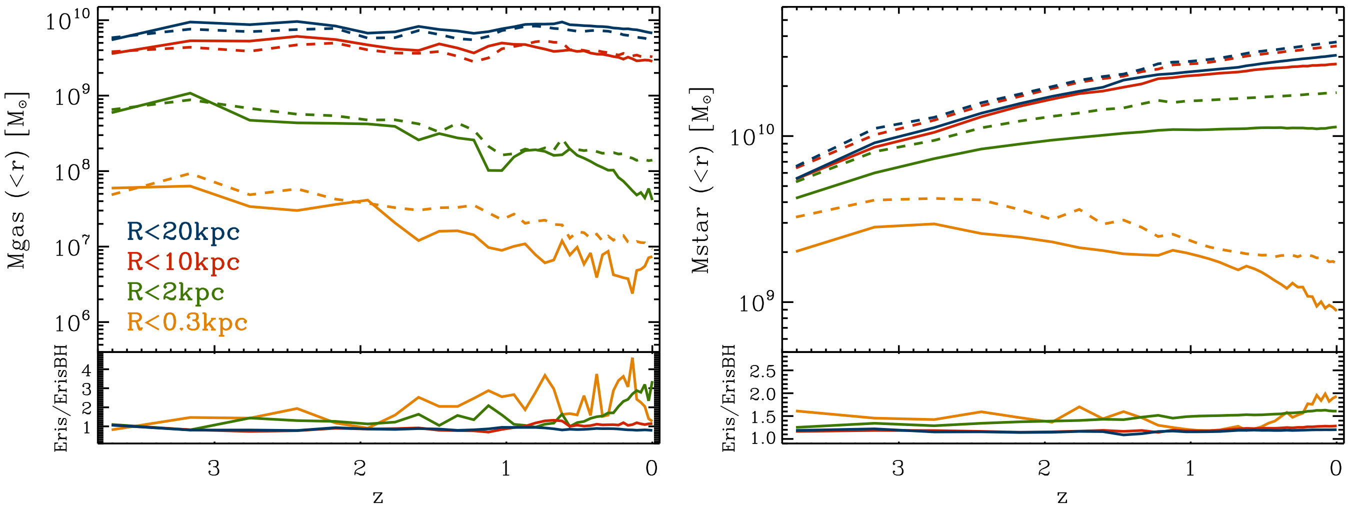

Figure 8. Redshift evolution of the gas mass (left-hand panel) and the stellar mass (right-hand panel) enclosed within different radii from the galaxy centre, for Eris*BH* (solid lines), and for Eris (dashed lines). The bottom panels show the ratios between Eris and Eris*BH*.

input from supernovae, both of type Ia and II, is more than an order of magnitude higher than the energy input from the central black hole). Despite not playing any dramatic role in shaping the host galaxy, AGN feedback seems, however, to be able to keep the very central region of the galaxy hot, preventing the bulge to grow in the same way as in the original Eris. To isolate the effects of AGN feedback on the Eris*BH* galaxy, we compare the properties of its gaseous and stellar components directly with the Eris galaxy, where AGN feedback was not included.

4.1 Gas component

In the left-hand panel of Fig. 8 we show the redshift evolution of the total mass in gas of Eris and Eris*BH* within spheres of different radii from the galaxy centre. At high redshift (above $z \sim 0.5$), the gas content of the two simulations is very similar, except in the very inner region (yellow curves), where the gas budget of Eris*BH* is systematically lower than the one of Eris, a consequence of the weak feedback from the slowly growing black hole.

While at large radii the total mass in gas remains very similar in the two simulations down to the present time, in the inner 2 kpc of Eris*BH* (green curves) the amount of gas starts decreasing at low redshift and, by $z = 0$, it is about a third of the one of Eris. The steep decline in gas content at those scales starts around $z \sim 0.3$–0.4, which is when the strong bar visible in the galaxy at $z = 0$ starts forming (see next section); as the bar gets stronger, it 'clears' the centre of the galaxy of its gas content. An exception is the very central region (the inner few hundred parsecs, yellow curves), where the amount of gas slightly increases at those late times. The increment of gas mass in the centre of the galaxy results in a slight increase of the black hole accretion rate (see Fig. 3) as well as of the star formation rate (see Fig. 12).

In Fig. 9 we show density maps at $z = 0.5$ (upper panels) and $z = 0$ (lower panels) in a region of 18 kpc of radius around the centre of Eris*BH* (left column) and Eris (right column). The angle of projection is chosen so that the discs appear face-on. While, as just discussed, the total amount of gas at large scales is approximately the same in both simulations, gas appears to be more diffuse in the Eris*BH* galaxy, as also its stellar disc is larger than the one of Eris (see Section 4.2 for a quantitative estimate of the disc mass). But the most striking difference between the two simulations is probably the 'empty' region, of about 2.5 kpc of radius, in the centre of Eris*BH* at $z = 0$. This region has approximately the physical extent of the bar that has formed at $z \sim 0.3$ and that, as we mentioned above, by $z = 0$ has cleared the centre of the galaxy.

4.2 Stellar component

Fig. 10 shows maps of the stellar density projected face-on, for the same regions of Fig. 9. At $z = 0.5$ the main differences between the two simulations are the slightly larger disc and the smaller bulge of Eris*BH*. It is again at $z = 0$ where we see the most remarkable differences between the two simulations: in Eris*BH* the bulge is not only smaller than the one of Eris, but now it also features a strong bar, clearly visible in the map, which has a radius of about 3 kpc. The presence of the bar causes the bulge to have a boxy-peanut morphology when viewed edge-on, as shown in Fig. 11.

As discussed in details in Guedes et al. (2013), the pseudobulge of Eris is the result of an inside-out growth, mainly evolved from a stellar bar that formed at high redshift and that has progressively weakened after $z = 1$. In Eris*BH* the evolution at recent times is different: the weak AGN feedback has inhibited the growth of the bulge, while its disc has actually grown to a larger size with respect to Eris. Being the disc larger and the bulge smaller (and thus with less stabilizing power), the disc of Eris*BH* is more prone to instabilities. While the bar of Eris thus progressively weakens after $z = 1$, in Eris*BH* the disc becomes again unstable at $z \sim 0.3$[6] and the bar gains again strength with several consequences for the stellar and gas properties (e.g. Figs 9, 12, 13).

The stellar density profiles of Eris*BH* and Eris are shown in Fig. 14, together with the best-fits for the bulge and disc components. The profiles have been fitted with a double Sérsic

[6] the ratio $v_{\rm peak}/\sqrt{GM_{\rm d}/R_d}$ (where $v_{\rm peak}$ is the peak of the circular velocity and $M_{\rm d}$ and R_d are the mass and scalelength of the disc) is traditionally used to estimate the stability of galactic discs (Mo, Mao & White 1998). Simulations show that a disc becomes unstable when this ratio becomes smaller than 1.1. We find that, at $z = 0.3$, Eris*BH* has precisely a value of 1.1, while, for comparison, Eris has a value of 1.4. Those numbers are consistent with the disc of Eris*BH* being about to become unstable, while Eris does not suffer any instability event.

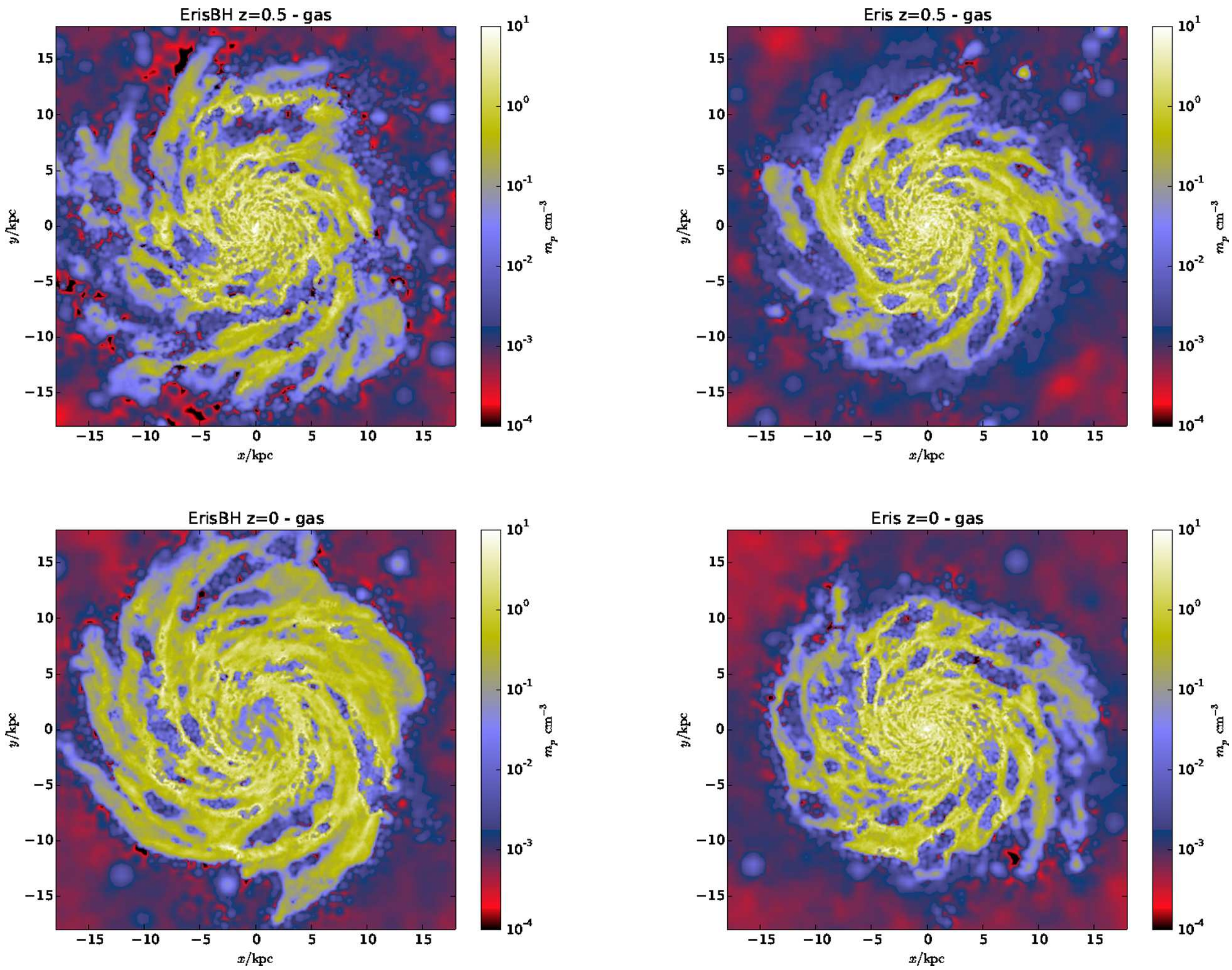

Figure 9. Gas density maps at $z = 0.5$ (upper panels) and at $z = 0$ (lower panels) for Eris*BH* (left) and Eris (right).

profile, with the Sérsic index for the bulge left unconstrained, and the one for the disc fixed at 1 (exponential disc). The best values for the fits are given in Table 2. The bulge of Eris*BH* features a smaller Sérsic index than Eris ($n_s = 0.9$ and $n_s = 1.2$, respectively), with a value lower than unity, typical of boxy bulges. The scale radius of the disc of Eris*BH* is instead larger than the one of Eris ($R_{\rm disc} = 2.9$ and $R_{\rm disc} = 2.3$, respectively). We obtained the total bulge and disc masses by integrating the Sérsic profiles, and got the values given in Table 2: the bulge of Eris*BH* is almost half the one of Eris, while the disc is slightly larger. As discussed above, the weak AGN feedback is responsible for the lower reservoir of gas in the central few hundred parsecs of Eris*BH* compared to Eris and the consequent lower star formation rate and stellar content in the central region of the galaxy. We note that the values we obtained here for the Sérsic index of the bulge and the scale radii for Eris differ from the ones given in Guedes et al. (2011). There, the fit was performed with the GALFIT (Peng et al. 2002) code run on the surface brightness profile obtained after processing the simulated galaxy with SUNRISE (Jonsson 2006). Using this methodology, Guedes et al. (2011) obtained a photometric B/D ratio of 0.35 in the *B*-band, lower of about a factor of 2 than the B/D ratio we obtain here for Eris. Assuming that for Eris*BH* the ratio between the photometric B/D ratio and the B/D ratio as we calculated here is the same as for Eris (which is plausible, given the similar stellar ages at galaxy scales between the two simulations, see Fig. 13), we estimate the photometric *B*-band B/D ratio of Eris*BH* to be 0.19, which would classify the galaxy as a barred *Sc* spiral.

We now look at the differences in SFR history between the two simulations. The evolution of the SFR of Eris and Eris*BH* if shown in Fig. 12. The largest differences between the two simulations are in the inner few kpc, where the star formation rate can be up to an order of magnitude lower in Eris*BH* than in Eris. This is reflected in the stellar distribution, which is shown in the right-hand panel of Fig. 8: within few kpc the stellar content in Eris*BH* can be up to 50 per cent lower than in Eris, while above 10 kpc there are no striking differences between the two simulations.

Apart for being generally lower in the central regions, the SFR in Eris*BH* has also a different redshift evolution: while in Eris the SFR gradually decreases after $z = 1$, in Eris*BH* we see still some small bursts of star formation at more recent times. There is particularly a new increase of star formation at $z < 0.3$, which is when the stellar bar is growing in strength. As the bar grows, it drives a new inflow of gas to the centre (see also the gas distribution in the central kpc in the left-hand panel of Fig. 8), which leads to a new episode of star formation.

The presence of a young generation of stars in the very centre of Eris*BH* can be seen also in Fig. 13, where we show the age distribution of the stars within different radial shells from the centre. The very central stars (within 300 pc) of Eris*BH* (solid histogram in the top-left panel) are primarily quite old, except for a population

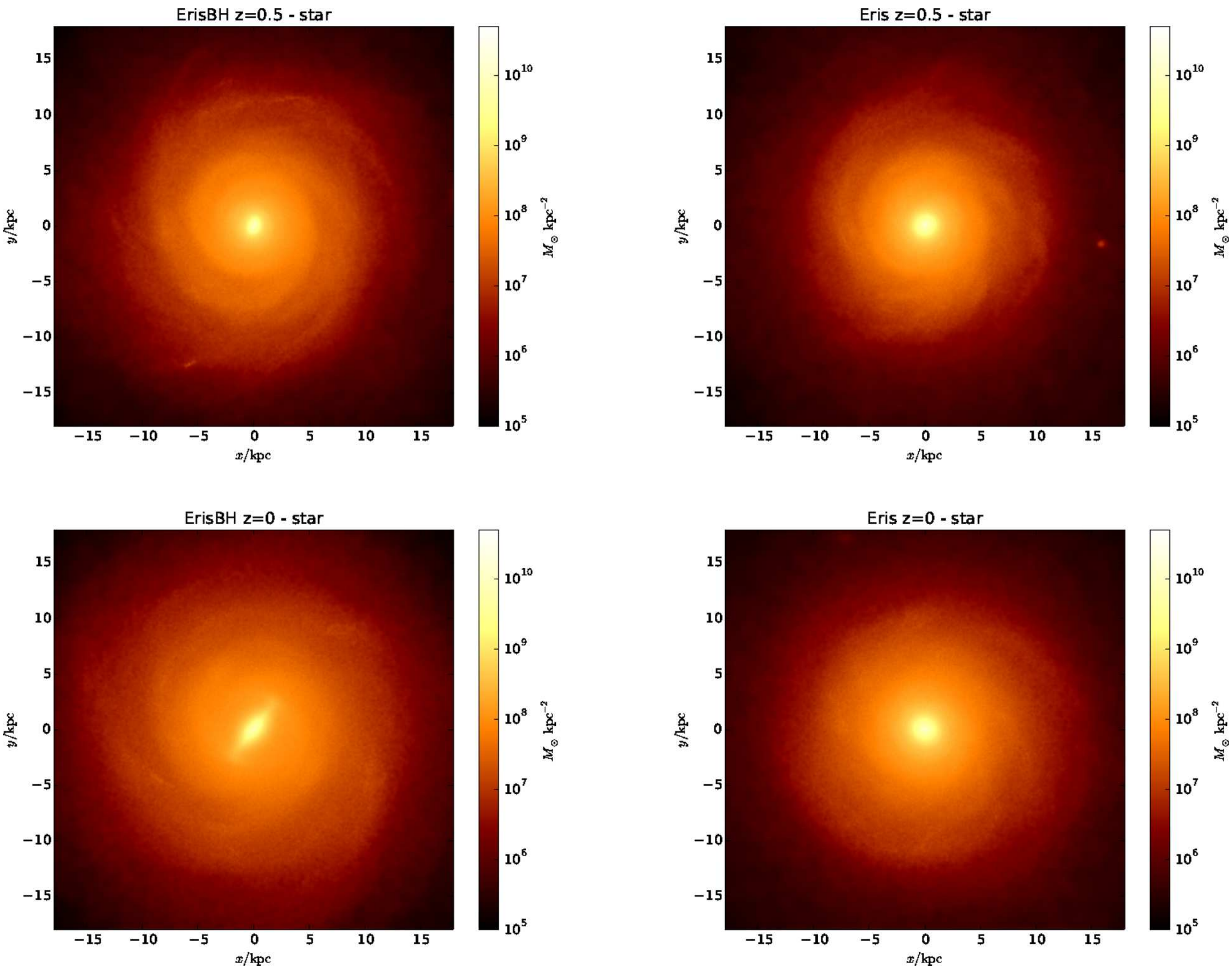

Figure 10. Star density maps at $z = 0.5$ (upper panels) and at $z = 0$ (lower panels) for Eris*BH* (left) and Eris (right).

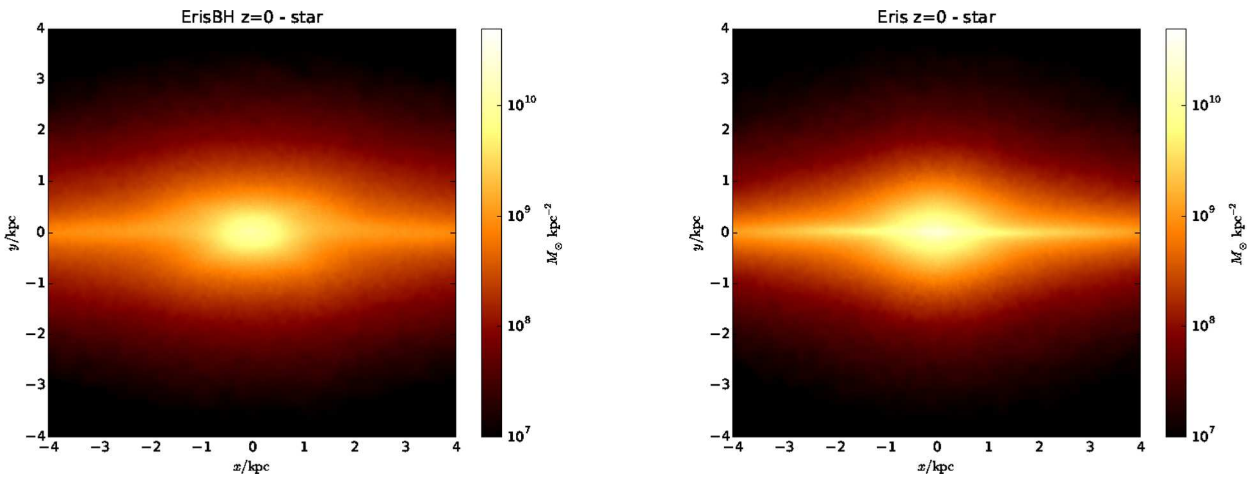

Figure 11. Zoom into the central region of Eris*BH* (left) and Eris (right) at $z = 0$, now viewed with the disc edge-on.

of young stars (age < 2 Gyr) originating from the new episode of star formation at $z < 0.3$ which takes place during the formation of the bar. In Eris (dotted histogram) the age distribution in the inner region is different: there is a large population of stars born during the last merger at $z \sim 1$ (age ~ 7 Gyr), and a slowly decreasing distribution at younger ages (see the corresponding increase in the SFR in the inner region around $z \sim 1$ in Fig. 12, followed by a gradual decrease of the SFR). These results suggest that barred galaxies are likely to host a young population of stars. This would be be qualitatively consistent with the results of Coelho & Gadotti (2011), who compared the stellar ages of a large sample of barred and unbarred galaxies with available spectra from the Sloan Digital Sky Survey, and found an excess of young stars (age < 4 Gyr) in bulges of barred galaxies compared to bulges of unbarred galaxies.

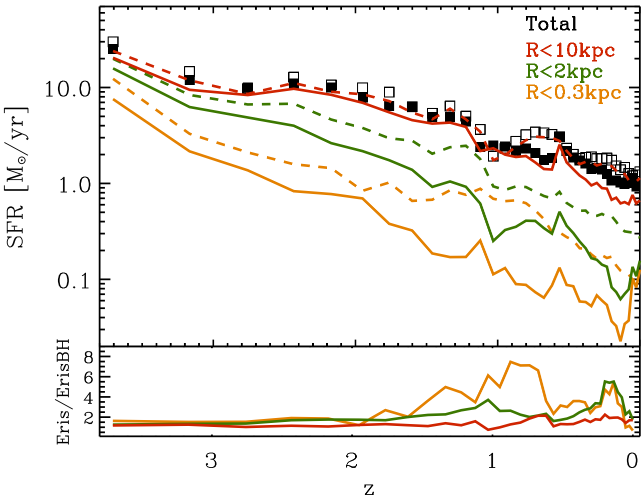

Figure 12. Comparison between the star formation history of Eris*BH* (solid squares) and Eris (empty squares). The black symbols show the evolution of the total SFR ($M_{\odot}$ yr^{-1}) in the simulation, while the coloured symbols show the SFR within a given radius from the centre of the galaxy, as indicated in the legend.

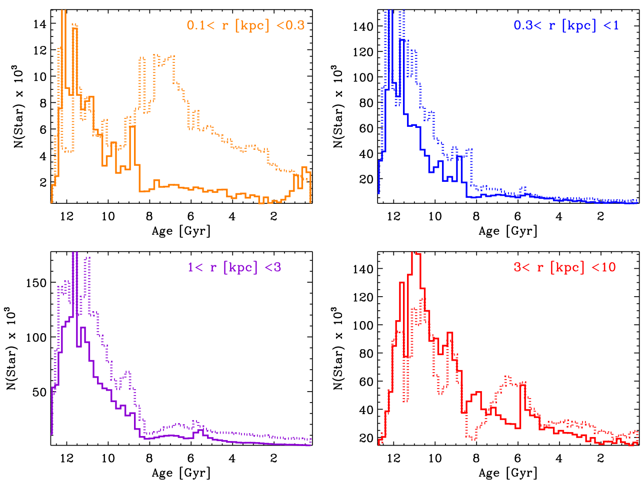

Figure 13. Age distribution of stars located, at $z = 0$, in shells with radial distance from the galaxy centre as indicated in the legend. Solid lines are for Eris*BH* and the dotted ones for Eris.

On top of causing a new inflow of gas which leads to the new burst of star formation, the bar has also a dynamical effect in the distribution of the stellar angular momentum in the centre of the galaxy. We study this by looking at the distribution of the 'orbital circularity parameter', often used to kinematically separate disc and bulge stars. The parameter is given by the ratio $j_z/j_{\rm circ}$, where j_z is the angular momentum of each star in the z-direction (after the galaxy has been rotated, so that the z-axis lies along the direction defined by the total angular momentum of all the gas particles in the galaxy), and $j_{\rm circ}$ is the angular momentum expected for a circular orbit at the radius of the star ($j_{\rm circ} = rv_{\rm circ}$, where $v_{circ}(r) = \sqrt{GM(r)/r}$). By definition, stellar discs, which are supported by rotation, have $j_z/j_{\rm circ} \sim 1$, while bulges dominated by velocity dispersion have $j_z/j_{\rm circ} \sim 0$. Fig. 15 shows the distribution of $j_z/j_{\rm circ}$ for Eris*BH* (left) and Eris (right) at $z = 0$ for all stars within 20 kpc from the centre (black curves) and for stars within different radii from the centre (coloured lines). Starting from the very central kpc (blue dotted curves), there is a striking difference between Eris*BH* and

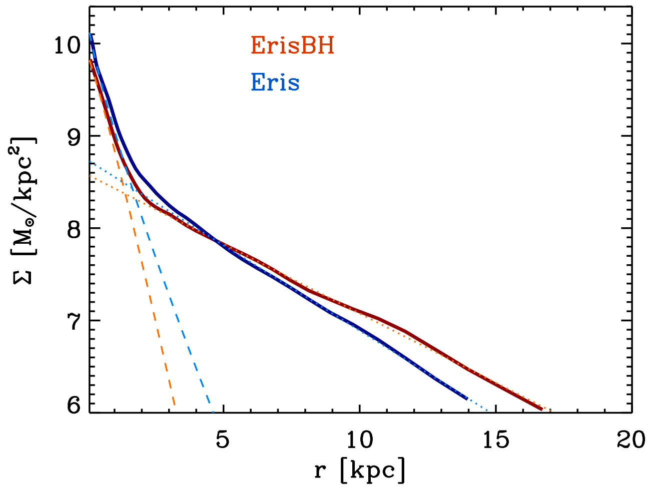

Figure 14. Stellar density profiles of Eris*BH* and Eris at $z = 0$ (solid lines). The two-components Sérsic fits are shown by the dashed and dotted curves, for the bulge and disc, respectively. The values of the best-fitting parameters are given in Table 2.

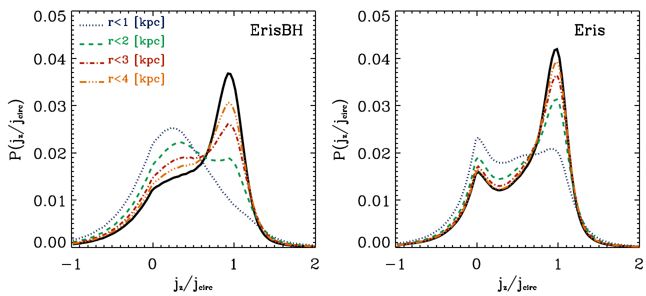

Figure 15. Distribution of 'orbital circularity parameter' $j_z/j_{\rm circ}$ for Eris*BH* (left-hand panel) and Eris (right-hand panel) at $z = 0$. The distribution including all stars within 20 kpc from the centre is given by the black lines. The coloured lines show the distribution for stars within spheres with radial distance from the centre as indicated in the legend.

Eris: in Eris (right-hand panel) there is a narrow peak of stars around $j_z/j_{\rm circ} = 0$, and a significant fraction of higher angular momentum particles that has reached the central region. This is not happening in Eris*BH*, where no clear peak at $j_z/j_{\rm circ} = 0$ is present and no high angular momentum stars are present in the centre of the galaxy (consistent with the presence of a strong bar). Moreover, in Eris the distribution of $j_z/j_{\rm circ}$ at $r \sim 2$ kpc has already the double-peaked shape typical of galaxies composed by a rotationally supported disc and a velocity dispersion-dominated bulge, while in Eris*BH* the distribution of $j_z/j_{\rm circ}$ at different radii shows a much slower transition, and only above 3 kpc (which is the approximate scale of the bar), $j_z/j_{\rm circ}$ is distributed as it does at large scales. A more detailed analysis of the effects that the bar has on the dynamical properties of the galaxy will be the subject of a separate paper.

Finally, the lower stellar content in the centre of Eris*BH* results to a lower rotation curve, with respect to Eris, in the inner 10 kpc (Fig. 16). A value around 190–200 km s^{-1} for the peak of the circular velocity in the inner region of the galaxy is consistent with the values estimated for the Milky Way by Portail et al. (2015), who constructed dynamical models of the bulge of the Galaxy using the 3D density measurements of Red Clump Giants and kinematic data from the BRAVA survey (Rich et al. 2007). At large distances, on the other side, the rotation curves of the two simulations are almost

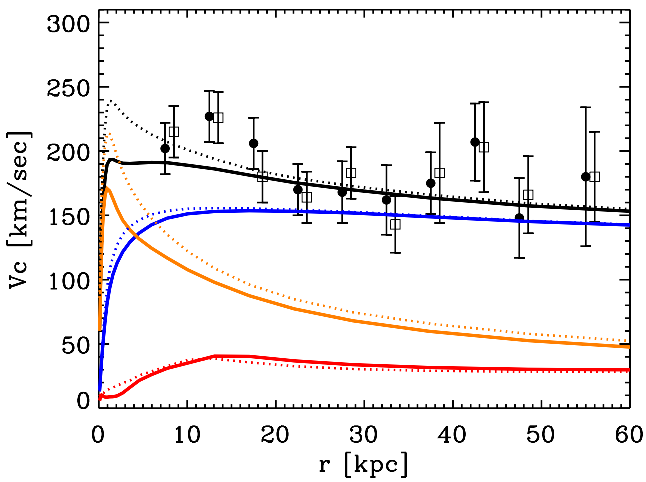

Figure 16. Rotation curves for Eris*BH* (solid lines) and Eris (dotted lines) in the inner 60 kpc. Total V_c (black curves), for dark matter only (blue curves), for stars only (orange curves), for gas only (red curves). The data points are from Xue et al. (2008).

identical, and consistent with the data of Xue et al. (2008), who estimated the Milky Way's rotation curve using the kinematics of blue horizontal-branch stars.

To conclude, despite being quantitatively modest, the feedback from the central black hole leads to small changes in the distribution of gas and stars in the inner region of the Eris*BH* galaxy, when compared to the Eris simulation (where AGN feedback was neglected). Those small variations are the origin of important secondary effects, particularly in the stability of the galaxy. Eris*BH*, in fact, experiences a strong instability at $z \sim 0.3$, which leads to the formation of a new large bar. The growth of the bar causes a modest inflow of gas to the very central region of the galaxy which leads to a small burst of star formation in the inner few hundred parsecs and a small increase of the black hole accretion rate. By $z = 0$, the central 2 kpc of the galaxy have been depleted of gas and the bulge, smaller than the bulge of Eris, has a boxy/peanut morphology typical of barred-galaxies.

5 SUMMARY AND CONCLUSIONS

In this paper we presented Eris*BH*, a new zoom-in cosmological simulation where we followed the evolution of a Milky Way-size dark matter halo with its baryon content from $z \sim 90$ to the present time. Eris*BH* is a twin simulation of Eris (Guedes et al. 2011), with which it shares the same initial conditions, simulated physical processes and the resolution of 120 pc, but, differently from Eris, it includes also prescriptions for the formation and evolution of massive black holes.

Four black holes are inserted during the simulation run in the most massive galaxies that also contain a large gaseous high-density region. The largest black hole, located in the largest galaxy of the simulated volume, is seeded at $z \sim 8.5$ with an initial mass of about $9 \times 10^5\ \mathrm{M_\odot}$.

In this first paper on Eris*BH* we focused on studying the properties of this central black hole, its growth, and its relation and influence on the host galaxy. Our main conclusions are:

(i) During its evolution, very little gas reaches the centre of the main galaxy, thus little fuel is available for feeding the central black hole, whose growth is generally highly sub-Eddington. Ending up at $z = 0$ with a mass of 2.6 million Solar masses, only ∼3 times its initial value, the black hole grows primarily (about a factor of 2) through mergers with the infalling black holes originally hosted by satellite galaxies;

(ii) Given the little gas supply, the value of the initial seed mass is rather important. Generalizing our results, we expect Milky Way-size galaxies to be hosting an intermediate-mass black hole already at $z \sim 8$. This could be possible either via a direct collapse in the protogalaxy, or via the uninterrupted growth close to the Eddington rate of a Pop III star remnant. Even very short phases of accretion close to the Eddington limit might make these black holes visible to the next generation of space telescopes, such as *JWST*;

(iii) The final black hole sits on the M_{BH}–σ and M_{BH}–M_{Bulge} relations in a location close to the one of SgrA*. Consistent with observational results for pseudobulges, Eris*BH* is close to the extrapolation at lower masses of the M_{BH}–σ relation established by more massive galaxies, while it is almost an order of magnitude below the M_{BH}–M_{Bulge} relation;

(iv) As the central black hole grows very little by gas accretion, AGN feedback is rather weak. Only the very central region of the galaxy seems to be affected by the presence of the black hole, with the consequence that only the gas content and the star formation rates in the central ∼1–2 kpc are lower than the ones found in Eris;

(v) Because of its smaller bulge and the lower concentration of gas in the centre, the disc of Eris*BH* is more unstable. The last instability event, at $z \sim 0.3$, causes the formation of a bar of about 3 kpc in radius and a burst of star formation in the very central few hundred parsecs;

(vi) At $z = 0$, the disc of Eris*BH* is slightly larger than the one of Eris, while its bulge is almost a factor of two smaller. Consequently, the B/D ratio of Eris*BH* is about half the one of Eris and its rotation curve flatter. Moreover, the bulge of Eris*BH* is characterized by the box/peanut morphology typical of barred galaxies, and, at its very centre, it hosts a population of very young stars.

In summary, as expected, progenitors of late-type galaxies seem to not be favourable sites for efficient black hole growth, probably due to their rather quiet merger history. While we do not witness any dramatic episode of AGN feedback, we find, however, that the weak, but circumscribed, energy input from the black hole helps the global stellar feedback to inhibit the growth of the bulge, which has important consequences on the global stability of the disc. Modest size black holes, though, might play an important role in the dynamical evolution of late-type spirals.

ACKNOWLEDGEMENTS

We thank Massimo Dotti, Dimitri Gadotti and Ortwin Gerhard for useful discussions. We also thank the anonymous referee for the careful reading of the manuscript and the useful suggestions which have improved its quality. This work was possible thanks to the computing time allocations at the Swiss National Supercomputing Center and at the Ohio Supercomputer Center. PM acknowledges support by the NSF through grant AST-1229745 and by NASA through grant NNX12AF87G. FG acknowledges support from NSF grant AST-0607819 and NASA ATP NNX08AG84G.

REFERENCES

Agarwal B., Khochfar S., Johnson J. L., Neistein E., Dalla Vecchia C., Livio M., 2012, MNRAS, 425, 2854
Agertz O., Kravtsov A. V., 2015, ApJ, 804, 18
Aumer M., White S. D. M., Naab T., Scannapieco C., 2013, MNRAS, 434, 3142

Baganoff F. K. et al., 2003, ApJ, 591, 891
Bellovary J. M., Governato F., Quinn T. R., Wadsley J., Shen S., Volonteri M., 2010, ApJ, 721, L148
Bellovary J. M. et al., 2014, MNRAS, 445, 2667
Bond J. R., Arnett W. D., Carr B. J., 1984, ApJ, 280, 825
Bondi H., 1952, MNRAS, 112, 195
Bondi H., Hoyle F., 1944, MNRAS, 104, 273
Bonoli S., Mayer L., Callegari S., 2014, MNRAS, 437, 1576
Booth C. M., Schaye J., 2009, MNRAS, 398, 53
Brook C. B. et al., 2011, MNRAS, 415, 1051
Callegari S., Mayer L., Kazantzidis S., Colpi M., Governato F., Quinn T., Wadsley J., 2009, ApJ, 696, L89
Callegari S., Kazantzidis S., Mayer L., Colpi M., Bellovary J. M., Quinn T., Wadsley J., 2011, ApJ, 729, 85
Chapon D., Mayer L., Teyssier R., 2013, MNRAS, 429, 3114
Churazov E., Sunyaev R., Forman W., Böhringer H., 2002, MNRAS, 332, 729
Churazov E., Sazonov S., Sunyaev R., Forman W., Jones C., Böhringer H., 2005, MNRAS, 363, L91
Coelho P., Gadotti D. A., 2011, ApJ, 743, L13
Debattista V. P., Mayer L., Carollo C. M., Moore B., Wadsley J., Quinn T., 2006, ApJ, 645, 209
Di Matteo T., Springel V., Hernquist L., 2005, Nature, 433, 604
Di Matteo T., Colberg J., Springel V., Hernquist L., Sijacki D., 2008, ApJ, 676, 33
Dijkstra M., Ferrara A., Mesinger A., 2014, MNRAS, 442, 2036
Dubois Y., Gavazzi R., Peirani S., Silk J., 2013, MNRAS, 433, 3297
Erwin P., Gadotti D. A., 2012, Adv. Astron., 2012, 4
Gadotti D. A., Kauffmann G., 2009, MNRAS, 399, 621
Ghez A. M. et al., 2008, ApJ, 689, 1044
Gill S. P. D., Knebe A., Gibson B. K., 2004, MNRAS, 351, 399
Gillessen S., Eisenhauer F., Trippe S., Alexander T., Genzel R., Martins F., Ott T., 2009, ApJ, 692, 1075
Governato F. et al., 2010, Nature, 463, 203
Graham A. W., Scott N., 2015, ApJ, 798, 54
Greene J. E., Ho L. C., Barth A. J., 2008, ApJ, 688, 159
Guedes J., Madau P., Mayer L., Callegari S., 2011, ApJ, 729, 125
Guedes J., Mayer L., Carollo M., Madau P., 2013, ApJ, 772, 36
Guo Q. et al., 2011, MNRAS, 413, 101
Haiman Z., Hui L., 2001, ApJ, 547, 27
Häring N., Rix H.-W., 2004, ApJ, 604, L89
Ho L. C., 2009, ApJ, 699, 626
Hopkins P. F., Quataert E., 2010, MNRAS, 407, 1529
Hopkins P. F., Quataert E., 2011, MNRAS, 415, 1027
Hopkins P. F., Robertson B., Krause E., Hernquist L., Cox T. J., 2006, ApJ, 652, 107
Hoyle F., Lyttleton R. A., 1939, in Proc. Cambridge Philosophical Society Vol. 35, Proceedings of the Cambridge Philosophical Society, p. 405
Hu J., 2008, MNRAS, 386, 2242
Jiang Y.-F., Greene J. E., Ho L. C., 2011, ApJ, 737, L45
Johnson J. L., Khochfar S., Greif T. H., Durier F., 2011, MNRAS, 410, 919
Jonsson P., 2006, MNRAS, 372, 2
Kaufmann T., Mayer L., Wadsley J., Stadel J., Moore B., 2007, MNRAS, 375, 53
King A., 2003, ApJ, 596, L27
Knollmann S. R., Knebe A., 2009, ApJS, 182, 608
Kormendy J., 2004, in Ho L. C., ed., Coevolution of Black Holes and Galaxies The Stellar-Dynamical Search for Supermassive Black Holes in Galactic Nuclei. p.
Kormendy J., Bender R., Cornell M. E., 2011, Nature, 469, 374
Kroupa P., 2001, MNRAS, 322, 231
Lemson G., Virgo Consortium the, 2006, preprint (arXiv:astro-ph/0608019)
Lodato G., Natarajan P., 2006, MNRAS, 371, 1813
McConnell N. J., Ma C.-P., 2013, ApJ, 764, 184
Madau P., Rees M. J., 2001, ApJ, 551, L27
Madau P., Haardt F., Dotti M., 2014, ApJ, 784, L38
Magorrian J. et al., 1998, AJ, 115, 2285
Marinacci F., Pakmor R., Springel V., 2014, MNRAS, 437, 1750
Martizzi D., Teyssier R., Moore B., 2012, MNRAS, 420, 2859
Martizzi D., Jimmy Teyssier R., Moore B., 2014, MNRAS, 443, 1500
Mathur S., Fields D., Peterson B. M., Grupe D., 2012, ApJ, 754, 146
Mayer L., Kazantzidis S., Madau P., Colpi M., Quinn T., Wadsley J., 2007, Science, 316, 1874
Mayer L., Kazantzidis S., Escala A., 2008, preprint (arXiv:e-prints)
Mayer L., Kazantzidis S., Escala A., Callegari S., 2010, Nature, 466, 1082
Mayer L., Fiacconi D., Bonoli S., Quinn T., Roškar R., Shen S., Wadsley J., 2015, ApJ, 810, 51
Merloni A., Heinz S., 2008, MNRAS, 388, 1011
Merritt D., Ferrarese L., 2001, ApJ, 547, 140
Mo H. J., Mao S., White S. D. M., 1998, MNRAS, 295, 319
Murante G., Monaco P., Borgani S., Tornatore L., Dolag K., Goz D., 2015, MNRAS, 447, 178
Narayan R., Mahadevan R., Grindlay J. E., Popham R. G., Gammie C., 1998, ApJ, 492, 554
Navarro J. F., Benz W., 1991, ApJ, 380, 320
Okamoto T., 2013, MNRAS, 428, 718
Pavlinsky M. N., Grebenev S. A., Sunyaev R. A., 1994, ApJ, 425, 110
Peng C. Y., Ho L. C., Impey C. D., Rix H.-W., 2002, AJ, 124, 266
Portail M., Wegg C., Gerhard O., Martinez-Valpuesta I., 2015, MNRAS, 448, 713
Regan J. A., Haehnelt M. G., 2009, MNRAS, 396, 343
Rich R. M., Reitzel D. B., Howard C. D., Zhao H., 2007, ApJ, 658, L29
Roškar R., Teyssier R., Agertz O., Wetzstein M., Moore B., 2014, MNRAS, 444, 2837
Roškar R., Fiacconi D., Mayer L., Kazantzidis S., Quinn T. R., Wadsley J., 2015, MNRAS, 449, 494
Scannapieco C. et. al, 2012, MNRAS, 423, 1726
Schaye J. et al., 2015, MNRAS, 446, 521
Shakura N. I., Sunyaev R. A., 1973, A&A, 24, 337
Sijacki D., Springel V., 2006, MNRAS, 366, 397
Sijacki D., Vogelsberger M., Genel S., Springel V., Torrey P., Snyder G. F., Nelson D., Hernquist L., 2015, MNRAS, 452, 575
Silk J., Rees M. J., 1998, A&A, 331, L1
Skinner G. K., Willmore A. P., Eyles C. J., Bertram D., Church M. J., 1987, Nature, 330, 544
Spergel D. N. et al., 2007, ApJS, 170, 377
Springel V., Di Matteo T., Hernquist L., 2005a, MNRAS, 361, 776
Springel V., Di Matteo T., Hernquist L., 2005b, ApJ, 620, L79
Stinson G., Seth A., Katz N., Wadsley J., Governato F., Quinn T., 2006, MNRAS, 373, 1074
Tanaka T., Haiman Z., 2009, ApJ, 696, 1798
Taylor P., Kobayashi C., 2014, MNRAS, 442, 2751
Tremaine S. et al., 2002, ApJ, 574, 740
Tremmel M., Governato F., Volonteri M., Quinn T. R., 2015, MNRAS, 451, 1868
Volonteri M., Bellovary J., 2012, Rep. Prog.Phys., 75, 124901
Volonteri M., Lodato G., Natarajan P., 2008, MNRAS, 383, 1079
Volonteri M., Silk J., Dubus G., 2015, ApJ, 804, 148
Wadsley J. W., Stadel J., Quinn T., 2004, New Astron., 9, 137
Wise J. H., Turk M. J., Abel T., 2008, ApJ, 682, 745
Wyithe J. S. B., Loeb A., 2012, MNRAS, 425, 2892
Xue X. X. et al., 2008, ApJ, 684, 1143

This paper has been typeset from a TEX/LATEX file prepared by the author.